Temperature–Moisture Dependence of the Deep Convective Transition as a Constraint on Entrainment in Climate Models

SANDEEP SAHANY, J. DAVID NEELIN, AND KATRINA HALES

Department of Atmospheric and Oceanic Sciences, University of California, Los Angeles, Los Angeles, California

RICHARD B. NEALE

National Center for Atmospheric Research, Boulder, Colorado

(Manuscript received 21 June 2011, in final form 5 October 2011)

ABSTRACT

Properties of the transition to strong deep convection, as previously observed in satellite precipitation statistics, are analyzed using parcel stability computations and a convective plume velocity equation. A set of alternative entrainment assumptions yields very different characteristics of the deep convection onset boundary (here measured by conditional instability and plume vertical velocity) in a bulk temperature–water vapor thermodynamic plane. In observations the threshold value of column water vapor above which there is a rapid increase in precipitation, referred to as the critical value, increases with temperature, but not as quickly as column saturation, and this can be matched only for cases with sufficiently strong entrainment. This corroborates the earlier hypothesis that entraining plumes can explain this feature seen in observations, and it places bounds on the lower-tropospheric entrainment. Examination of a simple interactive entrainment scheme in which a minimum turbulent entrainment is enhanced by a dynamic entrainment (associated with buoyancy-induced vertical acceleration) shows that the deep convection onset curve is governed by the prescribed minimum entrainment. Results from a 0.5° resolution version of the Community Climate System Model, whose convective parameterization includes substantial entrainment, yield a reasonable match to satellite observations in several respects. Temperature–water vapor dependence is seen to agree well with the plume calculations and with offline simulations performed using the convection scheme of the model. These findings suggest that the convective transition characteristics, including the onset curve in the temperature–water vapor plane, can provide a substantial constraint for entrainment assumptions used in climate model deep convective parameterizations.

1. Introduction

With the move toward higher resolution in global models, one might hope that additional aspects of the precipitation-generating processes would improve. However, the interaction with traditional convective parameterizations can potentially become problematic, as the separation of scale between the grid size and convective plume size is reduced. There is a need for benchmarks that summarize statistics of fast time scale motions in a manner that is relevant for the large scale. The agenda here is to link a particular set of such benchmark statistics for deep convective onset from prior observational work (outlined below) with calculations of convective plume buoyancy similar to those used in convective parameterizations. This includes quantifying the dependence of deep convective onset on free-tropospheric moisture as well as providing a constraint on the entrainment assumptions. We thus begin with a brief review of background on each aspect.

A number of observational studies have indicated that moist convection is sensitive to free-tropospheric humidity (Austin 1948; Malkus 1954; Brown and Zhang 1997; Sherwood 1999; Parsons et al. 2000; Bretherton et al. 2004; Sherwood et al. 2003). Some of these findings have also been confirmed from recent numerical modeling studies using convection-allowing models (Tompkins 2001; Grabowski 2003; Derbyshire et al. 2004). The transition of convection from shallow clouds to deep cumulonimbus

Corresponding author address: J. David Neelin, Dept. of Atmospheric and Oceanic Sciences, University of California, Los Angeles, 405 Hilgard Ave., Los Angeles, CA 90095-1565.
E-mail: neelin@atmos.ucla.edu

DOI: 10.1175/JAS-D-11-0164.1

involves many complex effects, and its realistic representation in climate models is essential for an accurate simulation of rainfall statistics.

Many climate models find it difficult to simulate this shallow to deep convective transition. Derbyshire et al. (2004) reported that commonly used convection schemes are likely too insensitive to free-tropospheric humidity. While several factors may contribute, including separate shallow and deep convection schemes and coarse vertical resolution, one of the more significant of these is thought to be the entrainment profile used in the updraft cloud model. The entrainment assumptions used in a convection scheme can play an important role in its ability to simulate the observed transition to deep convection. Entrainment dilution has a strong effect on the estimated convective available potential energy (CAPE) and closure assumptions in convection parameterization (e.g., Zhang 2009). Specifically, the relative roles of boundary layer humidity and the free-tropospheric humidity can significantly change, based on entrainment assumptions. Consequently, the entrainment profile chosen for instability computations can strongly influence the estimated statistics of quasi-equilibrium. Lee et al. (2003) found that enforcing a minimum value of entrainment can yield a substantial increase in tropical intraseasonal variability. Given the importance of mixing assumptions in buoyancy computations, Neale et al. (2008) included the effect of entrainment dilution in the CAPE computation of the Zhang–McFarlane convection scheme used in the National Center for Atmospheric Research (NCAR) Community Atmosphere Model version 3.5 (CAM3.5) and noted substantial improvements in several aspects of tropical circulation. Bechtold et al. (2008) formulated the organized component of the total entrainment as a function of the environmental relative humidity and found improvements in rainfall simulation and tropical wave activity. Strong sensitivity to entrainment and other parameters affecting the onset of convection has been noted in Stainforth et al. (2005), Zhao et al. (2009), and Neelin et al. (2010). A number of studies have worked toward evaluating convective plume entrainment observationally (Raymond and Blyth 1986; Brown and Zhang 1997; Jensen and Del Genio 2006; Bacmeister and Stephens 2010; Luo et al. 2010) or via cloud-resolving modeling (Kuang and Bretherton 2006; Li et al. 2008; Romps and Kuang 2010) and one of the aims here will be to complement these approaches with independent criteria.

Examining the transition to strong convection at high time resolution, Peters and Neelin (2006, hereafter PN06) borrowed techniques from clustering transition systems in statistical physics and showed that they could be usefully employed to condense information about precipitation onset statistics and to show relations among properties. A key quantity is the value of the column water vapor (CWV) at which the transition to strong deep convection occurs, termed the critical CWV w_c. Neelin et al. (2009, hereafter NPH09) examined the dependence on tropospheric temperature of this CWV. Taking into account bulk measures of tropospheric temperature aided the collapse of a number of leading precipitation statistics to relatively simple dependences on CWV and w_c. The critical value for the onset of convection was found to increase roughly linearly with tropospheric temperature, but this dependence differed substantially from that of the most obvious rule of thumb, column saturation. At higher temperatures convective onset occurs at lower saturation across a set of tropical regions.

This paper will focus on explaining this behavior and linking it to entraining plume calculations in a single-plume framework such as can be used to constrain climate model convective parameterizations. It is thus worth reviewing an example of these results. Figure 1a shows precipitation retrievals conditionally averaged on CWV and a bulk tropospheric temperature. These are displayed as a function of CWV for various values of this bulk temperature. Here a tropospheric average temperature $\hat{T}$ (200–1000 hPa) is used (NPH09 obtained similar results for other measures). Such bulk measures are consistent with the use of CWV and permit analysis of the leading-order behavior of the moisture–temperature dependence of the onset of deep convection. Ideally one would like to carry out such estimates with additional vertical degrees of freedom but the approach makes use of the vast number of measurements available for CWV. Specifically, in Fig. 1a, microwave estimates of precipitation (for details see section 3) are conditionally averaged in $\hat{T}$ bins of 1 K and CWV bins of 0.3 mm, using temperature profiles from the National Centers for Environmental Prediction (NCEP)–National Center for Atmospheric Research (NCAR) reanalysis (Kalnay et al. 1996), and precipitation and CWV values from the Tropical Rainfall Measuring Mission (TRMM; Kummerow et al. 2000) Microwave Imager [TMI; processed by Remote Sensing Systems with the Hilburn and Wentz (2008) algorithm], over the tropical western Pacific. A rapid pickup in precipitation can be seen to occur at a value of CWV that differs for each $\hat{T}$. This value is referred to as the critical CWV (following the PN06 and NPH09 terminology). A nonlinear fitting of a power law above w_c allows an objective estimate of where the onset occurs. Specifically, the power-law fit is of the form $a(w - w_c)^\beta$ (following PN06 and NPH09), with $\beta = 0.185$ for all the curves.

Because w_c turns out to be an important measure, it is worth examining its dependence on temperature as shown

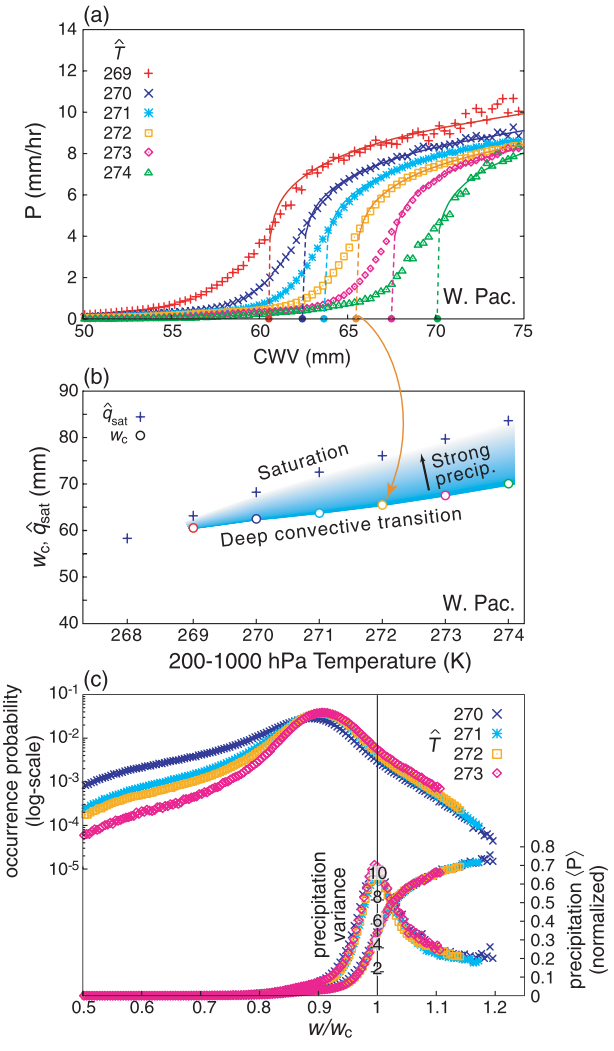

FIG. 1. (a) Conditionally averaged precipitation as a function of CWV for different bins of bulk tropospheric temperature $\hat{T}$ over the tropical western Pacific. Power-law fit lines (solid curves) of the form $a(w - w_c)^{\beta}$ are shown above the critical value w_c, where precipitation undergoes a rapid pickup (dashed lines connect the fit curves to the values of w_c on the axis). (b) Estimated values of w_c, defining an empirical estimate of the deep convective transition, as a function of $\hat{T}$. Also shown is the vertically integrated (200–1000 hPa) saturation specific humidity $\widehat{q_{\rm sat}}$. (c) Probability of occurrence of precipitating points, variance of precipitation, and normalized precipitation for the most populous $\hat{T}$ bins, as a function of rescaled CWV w/w_c.

in Fig. 1b. A natural thing to compare this to (Bretherton et al. 2004) is the column saturation value $\widehat{q_{\rm sat}}$, which is also shown as a function of $\hat{T}$ in Fig. 1b. The w_c values (estimated here using NCEP temperatures) are very close to those reported in NPH09 [where temperatures from the 40-yr European Centre for Medium-Range Weather Forecasts (ECMWF) Re-Analysis (ERA-40; Uppala et al. 2005) were used]. Figure 1b corroborates (with a different temperature dataset) the findings of NPH09 that at higher temperatures the deep convective onset tends to occur at lower values of relative humidity, as can be seen from the increasing distance of the onset boundary and the column saturation line with increasing temperatures. As in NPH09, similar results are found when the w_c estimation is carried out for different tropical regions (the western Pacific chosen here). The empirical critical value thus does not have a simple relation to the column saturation value—it is this property that we aim to explore in this paper.

To illustrate the usefulness of this critical value, Fig. 1c shows an example of how various statistics related to deep convection can be collapsed to similar dependences when CWV is rescaled. The probability of occurrence of CWV values (for precipitating points), variance of precipitation, and precipitation (normalized by an amplitude factor determined from the power-law fits) are shown as a function of CWV rescaled by the corresponding estimated w_c values (as in Neelin et al. 2008). The curves for different $\hat{T}$ tend to collapse to a common dependence on the rescaled variable w/w_c. Thus, the critical value of CWV seems to be a robust indicator of the transition to deep convection over the tropical oceans and can be useful in condensing properties of various statistical measures of precipitation.

To investigate physical mechanisms governing the CWV–precipitation relationship, Holloway and Neelin (2009, hereafter HN09), examined entraining plume buoyancy using sonde data from Nauru. Using various entrainment schemes, they found that higher values of CWV are associated with higher plume buoyancies, especially in the upper troposphere. Moisture content of the lower-tropospheric air was found to be particularly important for this buoyancy increase, by means of entrainment. Thus, highly entraining plumes were found to produce relationships between CWV and the onset of conditional instability, matching aspects of the observed onset of deep convection and precipitation. This paper further pursues this agenda under the hypothesis that the bulk temperature–CWV relationship seen in the observed convective transition can be explained by such plume models. Quantifying the relationship of the onset of deep convection in observations via the onset in entraining plume models potentially provides additional constraints for convective parameterization schemes. This also helps to establish whether onset statistics such as those seen in Fig. 1a can provide useful metrics for climate models.

A first step is to verify whether the observed transition boundary as a function of temperature and moisture can be reasonably reproduced by simple plume calculations and offline versions of convection schemes used in climate

models (section 2). In these calculations, conditional instability of a deep convective column and plume vertical velocity are used as representative measures of the onset of deep convection. For the computation of plume vertical velocity, an updraft velocity equation is coupled to the buoyancy calculation, with the caveat that the vertical pressure gradient term is ignored. Similar calculations were performed using an offline version of the Zhang–McFarlane convection scheme as modified by Neale and Richter (Neale et al. 2008; the scheme is hereafter referred to as ZMNR). Analysis of these parameters as a function of bulk measures of water vapor and temperature shows that the onset of deep convection is strongly influenced by the choice of entrainment formulation (section 3). To investigate if climate models can capture the temperature–moisture dependence of deep convective onset, we compare the model output from a high-resolution (0.5°) simulation of CAM3.5, with satellite observations (section 4). Agreement between the offline calculations using ZMNR and the high-resolution model output supports the use of the offline model to analyze the physics and sensitivity in a more controlled environment.

2. Buoyancy computation and the updraft equation

a. Buoyancy computation and entrainment cases

The buoyancy computations use the standard formulation:

$$r_k = (1 - \chi_{k-1}\Delta p)r_{k-1} + \chi_{k-1}\Delta p\tilde{r}_{k-1}, \qquad (1)$$

where r is a conserved variable, $\tilde{r}$ is the corresponding environmental value, k is the pressure level, Δp is the pressure interval (5 hPa), and χ denotes the mixing coefficient. For the buoyancy computations, a theoretical parcel is made to rise from the 1000-hPa level, conserving total water specific humidity q_t and the ice–liquid water potential temperature θ_{il}, with no precipitation production, and thus all the condensate is retained by the parcel in the form of cloud water (below the freezing level) and cloud ice (freezing level and above). For clarity a simple single-step water-to-ice conversion at the freezing level is used (which permits this contribution to be assessed visually in buoyancy profiles).

To examine the impact of entrainment formulations, a set of simple assumptions for the dependence of the mixing coefficients is examined. The following entrainment cases are considered (illustrated in the appendix):

(i) No entrainment. The mixing coefficient for entrainment of environmental air is set to zero for the entire atmospheric column. Properties of a rising parcel are determined by its temperature and moisture content at the level of initiation.

(ii) Constant entrainment. In this formulation the mixing coefficient has one value through the vertical column (50–950 hPa) above the atmospheric boundary layer (ABL), with a larger fixed value in the ABL (950–1000 hPa). To study the sensitivity of the plume calculations to the prescribed values of the mixing coefficient, four different profiles are used. In the ABL, all of them have the same value of the mixing coefficient ($0.18\ \text{hPa}^{-1} \approx 19.83\ \text{km}^{-1}$), whereas for the rest of the vertical column, the prescribed values are 0, 1, 2, and $4 \times 10^{-3}\ \text{hPa}^{-1}$ specified in pressure coordinates and these are thus referred to as C0, C1, C2, and C4, respectively. The corresponding values for C1, C2, and C4 are 0.1, 0.2, and $0.4\ \text{km}^{-1}$ in the lower troposphere (around 900 hPa), the conversions for p-coordinate values in the midtroposphere (around 500 hPa) are approximately 0.06, 0.12, and $0.24\ \text{km}^{-1}$, respectively, and in the upper troposphere (around 200 hPa), they are approximately 0.03, 0.06, and $0.12\ \text{km}^{-1}$, respectively. The lower-tropospheric values are similar to or moderately higher than those used by some convective parameterization schemes; for example, Tiedtke (1989) assumed an entrainment rate of $0.1\ \text{km}^{-1}$ for deep convective clouds and Brown and Zhang (1997) use similar values. A constant high value of the entrainment coefficient is used in the ABL in C0–C4 to make it clear that varying free-tropospheric entrainment is the dominant factor in results here. Sensitivity tests have also been conducted, for instance, using C4 values from 950 to 600 or 700 hPa and C2 values in the upper troposphere.

(iii) Modified version of the Zhang–McFarlane convection scheme (ZMNR). Neale et al. (2008) made modifications to the Zhang–McFarlane convection scheme used in the NCAR CAM3.5 by using a prescribed entrainment rate ($1\ \text{km}^{-1}$) for the CAPE computation, thus relaxing the assumption of a nondilute plume (no mixing with environmental air) in the standard Zhang and McFarlane (1995) version. The motivation for this change was primarily to alleviate the bias in the model-simulated near-surface thermodynamic conditions and to increase the sensitivity of deep convection to free-tropospheric humidity.

(iv) Deep inflow A (Deep A). This is similar to the LES-based estimate of the vertical dependence of the mixing coefficient reported in Siebesma et al. (2007). In this case, the plume mixes with the environmental air through a sufficiently deep layer in

the lower troposphere, unlike the constant entrainment case, where most of the mixing happens in the first few layers. The mixing coefficient in this formulation has an inverse dependence on height, and is given by the following relation (as in HN09):

$$\chi_k \Delta p = c_\epsilon z_k^{-1} \Delta z_k, \tag{2}$$

where χ_k is the mixing coefficient for layer k expressed in pressure coordinates (hPa^{-1}), Δp is the pressure interval between two consecutive vertical levels (5 hPa), Δz_k is the depth of the layer, and $c_\epsilon = 0.4$. In height coordinates, the mixing coefficient for Deep A has a value of almost 1 km^{-1} at 970 hPa, 0.39 km^{-1} at 900 hPa, and 0.06 km^{-1} at 500 hPa.

(v) Deep inflow B (Deep B). Similar to HN09, an idealized updraft vertical velocity profile is chosen such that it increases almost linearly at lower levels (in height coordinates), with zero at 1000 hPa (≈84 m) and maximum at 430 hPa (7 km). This is similar to the updraft velocities reported in Robe and Emanuel (1996), and some of the relevant observational studies (e.g., LeMone and Zipser 1980; Cifelli and Rutledge 1994; LeMone and Moncrieff 1994). The mixing coefficients are then computed from the vertical gradient of the specified updraft vertical velocity profile (noting that for this case, the specified profile is simply a means of roughly justifying the mixing profile, as opposed to the interactive mixing of case (vi) where the updraft profile changes). For simplicity, the mixing coefficient is set to zero above 430 hPa, since there is negligible increase in mass flux beyond this level. In height coordinates, the mixing coefficient for Deep B has a value of almost 2.8 km^{-1} at 970 hPa, and 1 km^{-1} at 900 hPa.

(vi) Interactive (dynamic) entrainment. Unlike the previous cases, where the mixing coefficient is fixed a priori and is thus independent of the evolution of the plume, in this case it is a function of the updraft vertical velocity and hence is, in part, dynamically determined, rather than being statically prescribed (e.g., HN09; de Rooy and Siebesma 2010). The total entrainment essentially consists of two components, namely the minimum prescribed value (turbulent entrainment) and the dynamic entrainment associated with buoyancy-induced vertical acceleration, as follows:

$$\chi_k = \chi_{\min} + \frac{(\omega_k - \omega_{k-1})}{\Delta p(\omega_k + \omega_{k-1})/2}, \tag{3}$$

where $\chi_{\min}$ is the minimum prescribed mixing and ω_k is the pressure vertical velocity for layer k [computed from the updraft vertical velocity; see Eq. (5)]. In the ABL (1000–950 hPa), entrainment is specified to be the same as Deep B (i.e., corresponding to assuming linear plume growth).

To explore the sensitivity of the plume calculations to the minimum prescribed value, we perform two sets of computations, one with a prescribed minimum of 0.002 hPa^{-1} and the other with 0.004 hPa^{-1}, denoted I2 and I4, respectively. Note that the minimum prescribed values for I2 and I4 are same as the free-tropospheric values used in C2 and C4 above.

In discussion we loosely group the C0 and non-entraining scheme as low entrainment and C2, I2, Deep A, C4, I4, and Deep B as high entrainment, with the caveat that the vertical structure differences must be taken into account when making finer distinctions (e.g., comparing C2 and C4, or Deep A and Deep B).

b. Updraft equation

The plume equation is used to diagnose updraft velocity both for analysis and also to test the interactive entrainment assumptions. Interactive or ''dynamic'' entrainment attempts to take into account effects of vertical acceleration of the plume that would enhance entrainment by a mass flux balance, assuming that turbulence prevents the width of the plume from decreasing (Houghton and Cramer 1951; Ferrier and Houze 1989; de Rooy and Siebesma 2010; HN09). To estimate the importance of such effects, we use a plume velocity equation similar to those used in prior studies (e.g., Simpson and Wiggert 1969; Sud and Walker 1999; Gregory 2001; Siebesma et al. 2007; Kim and Kang 2012) to diagnose updraft vertical velocity from buoyancy:

$$\frac{\partial w_u^2}{\partial z} = -\frac{c}{z} w_u^2 + aB, \tag{4}$$

where w_u is the updraft velocity, B is the buoyancy term, and c and a are constants. In the Simpson and Wiggert (1969) formulation, $a = 2/(1 + \gamma)$, with $\gamma > 0$, while Siebesma et al. (2007) make assumptions regarding the pressure gradient term such that the effects of buoyancy are actually enhanced (i.e., $a > 2$). We have done sensitivity tests with a from 1 to 3, but in fact the sensitivity can be more easily seen from the analytic solution below.

The plume velocity equation is treated as a separable add-on to the buoyancy calculations (note that the

buoyancy calculation does not have the same form as that of the plume equation for the vertical velocity). This is done in order to have a buoyancy computation that closely parallels the standard calculations that do not use a vertical velocity, while at the same time being able to explore some of the consequences for models where a plume velocity is calculated. The mixing coefficient for buoyancy is influenced by the vertical velocity only for the interactive entrainment cases.

A solution for this formulation of the updraft velocity is

$$w_u^2 = z^{-c}\int_0^z a\dot{z}^c B\, d\dot{z} + w_0^2\left(\frac{z}{z_0}\right)^{-c}, \tag{5}$$

where w_0 is the initial perturbation velocity and z_0 is the height where it is applied. This solution is similar to that of HN09, but with a second term on the rhs included. This term represents the initial perturbation to the updraft velocity of the plume due, for example, to propagating gust fronts initiated by convective downdrafts. Equivalently, one could define a perturbation pressure gradient through the layer of the gust front that would yield this vertical velocity at the top of the layer. For results shown, we have used a value of 10 m s^{-1} for w_0 and 350 m for z_0. Most of the observational studies on gust fronts have been done for the midlatitudes (e.g., Wakimoto 1982), and they report similar or higher values for the speed and depth, depending on the stage of development of the front.

From this solution it may be seen that increasing a by some factor f and increasing w_0 by the square root of f will leave the shape of the solution unchanged, although its amplitude will be proportional to f. Thus for instance whether or not a plume reaches the upper troposphere will be independent of a (with this corresponding change of w_0) because regions of negative and positive buoyancy rescale by the same factor. The amplitude also cancels in the calculation of the dynamic entrainment contribution, so for purposes here sensitivity to a is equivalent to sensitivity to independent changes in w_0 (aside from the amplitude of w_u, which is not presented). Results are shown for the case of $a = 1$. For the entrainment used here (a strong momentum entrainment case $c = 1$ is shown, though smaller values have been tested) the influence of w_0 drops off fairly rapidly with height [compared to, e.g., Gregory (2001) where the effects reach the upper troposphere], although w_0 is important to the plume punching through layers of negative buoyancy in the lower troposphere.

3. Transition to deep convection as a function of tropospheric temperature

In this section we explore the dependence of w_c, a measure of the transition to deep convection (PN06), on tropospheric temperature. As summarized in the introduction, NPH09 computed w_c over various tropical ocean basins, using the ERA-40 temperatures and the TMI column water vapor, exploring its dependence on bulk measures of tropospheric temperature. We compute w_c values over the western Pacific using the same method as that used in NPH09, but using temperature profiles from the NCEP–NCAR reanalysis. The w_c values thus computed are plotted as a function of CWV and $\hat{T}$ and shown in Fig. 1b. These are repeated in Fig. 2 in order to compare them to plume calculations below. Also shown in Fig. 2 are w_c values reported in NPH09 (which used ERA-40 temperatures). The slopes of the deep convective onset boundaries for the two temperature sources agree quite well, although the w_c values estimated using the NCEP temperature profiles are marginally higher than those estimated from the ERA-40 profiles. The critical value for the onset of convection has an approximately linear dependence on $\hat{T}$, increasing at a rate of about 2.2 mm K^{-1} in the range of temperatures analyzed. This change is approximately 3.6% K^{-1}, while the column saturation value increases at a rate of around 6% K^{-1}, emphasizing that the ratio of w_c to the column saturated value has a temperature dependence. To test if simple convective plume representations such as those used in current convective schemes can capture this behavior, and to improve our understanding of the physical mechanisms underlying the deep convective transition, we perform plume computations with different entrainment formulations and various assumptions for the vertical structure of temperature perturbations.

a. *Plume calculations using typical temperature profiles from ERA-40*

We select a set of temperature profiles typical of those for conditions that have a reasonable chance of deep convection from the ERA-40 dataset. For this, temperature profiles over the tropical western Pacific are first binned at 1-K intervals of corresponding $\hat{T}$ values. Then, for each bin, we choose only those temperature profiles that have a corresponding CWV value greater than $0.9w_c$ (w_c values for western Pacific reported in NPH09 have been used) for the given $\hat{T}$, and then compute the mean of all the conditioned profiles, such that the composite represents a typical temperature sounding conducive for deep convection. Plume computations then use these conditional mean profiles. The results can thus be interpreted in terms of this simple set of T soundings (as opposed to carrying out calculations for all T soundings and then averaging the results as was done in HN09). Similarly, we wish to have a simplified profile of relative humidity that maintains essential features of

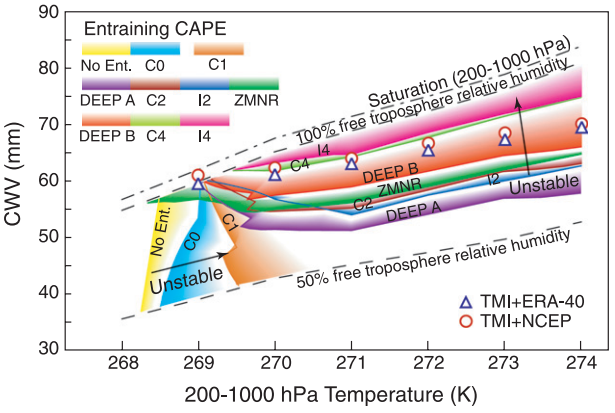

FIG. 2. The onset of conditional instability from parcel/plume calculations (see text) for different entrainment cases as a function of $\hat{T}$ is shown. Each line corresponds to an entraining CAPE contour of 100 J kg^{-1}, shown as a measure of the convective onset boundary analogous to the deep convective transition line shown in Fig. 1b. Values of w_c from Fig. 1b (estimated from TMI with NCEP temperatures) are shown as open circles for comparison (triangles show corresponding values using ERA-40 temperatures). For each entrainment scheme, shading indicates on which side of the contour convective instability increases (CAPE typically increases all the way to saturation; the shading is faded out to permit onset boundaries for other entrainment schemes to be shown). The constant entrainment cases C0, C1, C2, and C4 have coefficients of 0, 1, 2, and 4×10^{-3} hPa^{-1}, respectively, in the free troposphere. The interactive entrainment cases I2 and I4 have a minimum entrainment in the free troposphere corresponding to C2 and C4. The Deep A and Deep B cases have a vertical structure of the entrainment coefficient that has an approximate z^{-1} dependence in the lower troposphere.

observed moisture variations but with only 2 vertical degrees of freedom (characterizing free troposphere and ABL, respectively) for ease of interpretation. This also allows calculations to be easily continued into the very high free-tropospheric relative humidity range (which in observed profiles has smaller sample size). The idealized profile is chosen as follows. A typical surface relative humidity value for convective onset cases (85%) is prescribed, with a linear increase at 6.5% (50 hPa)$^{-1}$ up to 950 hPa, approximately matching observations for convecting or close-to-convecting cases (HN09). Above this a blending region has an interpolation to a constant free-tropospheric value above 800 hPa. This free-tropospheric relative humidity is varied through a range of 51%–99%. Plume calculations are performed for these T and q profiles of the environment, using in turn each of the entrainment cases listed in section 2a.

We wish to compare the convective onset boundary estimated in observations to a reasonable analog for each of these calculations. Neelin et al. (2008) analyzed the dependence of entraining CAPE on CWV [where the entraining CAPE $\int_{z_0}^{z_{\mathrm{LNB}}} \overline{T}_v^{-1} g(T_{vp} - \overline{T}_v)\, dz$ is calculated as for CAPE but replacing an adiabatic parcel virtual temperature by that of an entraining parcel T_{vp}, in this case with a constant mixing of 0.1% of environmental air per hectopascal, with $\overline{T}_v$ the virtual temperature of the environment]. They found a sharp pickup, similar to that seen in precipitation, in the entraining CAPE at sufficiently high CWV corresponding to the onset of deep convective cases. Thus, entraining CAPE can be used as a reasonable measure to characterize deep convective onset, although it comes with the caveat that the w_c value thus estimated might show marginal differences depending on the method of estimation. Figure 2 shows the deep convective onset boundary, using the 100 J kg^{-1} entraining CAPE contour as an estimator of the onset, for each of the entrainment cases, as a function of $\hat{T}$ and CWV. Sensitivity to the choice of entraining CAPE contour will be discussed below.

Consider one of the entrainment cases, Deep B, as an example. At a given $\hat{T}$ if one begins at low values of free-tropospheric relative humidity as indicated by low CWV values, this entrainment calculation yields convective stability. As one moves toward higher CWV, the onset of convective instability occurs. For each contour, shading indicates which side of the contour has increasing CAPE (i.e., on which side convective instability occurs). At different temperatures, the onset boundary as estimated by the 100 J kg^{-1} contour occurs at different column water vapor values. For this entrainment scheme, overall the onset boundary angles toward higher CWV at higher $\hat{T}$ in a manner that roughly parallels the onset as estimated from microwave precipitation observations. As one considers different entrainment cases, however, the onset boundary can shift substantially.

The shifts in the position and slope of the onset boundaries in Fig. 2 as one changes entrainment cases indicate that the relationship of the critical column water vapor to tropospheric temperature shows strong sensitivity to the entrainment formulation. For the nonentraining case, it can be seen from the figure that deep convection occurs over almost the entire range of $\hat{T}$ and CWV values used in this study. For the constant entrainment cases, the temperature dependence of w_c is found to be a strong function of the mixing coefficient value in the free troposphere. For the no entrainment and C0 cases, lower relative humidity soundings can be slightly more unstable because of the direct effect of water vapor on the density of air (i.e., the virtual temperature effect). These cases are highly unstable under circumstances for which the observations suggest that deep convection does not occur. As entrainment increases, the onset boundary rapidly changes to a configuration where instability increases for higher relative humidity because the entrained air has less negative impact on the buoyancy of the parcel.

Although the two deep-inflow cases are very similar in design, for a given temperature onset with Deep A starts at much lower values of free-tropospheric CWV than that of Deep B, which has stronger entrainment at a given level in the lower troposphere. In the case of interactive entrainment, the prescribed minimum value plays a significant role in governing the onset characteristics. For I2, deep convection starts at somewhat lower values of $\hat{T}$, as compared to I4. In addition, for a given value of $\hat{T}$, the critical CWV for I4 is found to be much higher than that for I2. An interactive entrainment case with no minimum entrainment (not shown) behaves much like the C0 case (with no free-tropospheric entrainment) in terms of onset boundary. This occurs because near the onset of conditional instability, there is little buoyancy to force vertical acceleration that could yield dynamic entrainment.

Overall, the high entrainment cases show a qualitative agreement with the observations, in terms of slope of the onset boundary. In terms of the w_c values estimated from CAPE, the set of C2, I2, Deep A, and Deep B, and the set of C4 and I4, bracket the observations. Note that the onset boundary for the high entrainment cases is at an angle to the constant RH line, such that for higher $\hat{T}$, deep convection occurs at lower values of free-tropospheric RH, consistent with the findings from observations and those reported in NPH09. Even at 100% free-tropospheric RH the highly entraining schemes do not show any deep convection for colder tropospheric temperatures, approximately reproducing this feature of the observations. Interestingly, the observed w_c–$\hat{T}$ relationship can be approximately captured even with a simple constant entrainment scheme, with the right choice of mixing-coefficient values, thus explaining to some extent the success of some of the cumulus parameterization schemes employing such entrainment formulations. We note that even when different entrainment formulations look similar on this onset diagram, they can have other measures that distinguish them. For instance, the Deep B case shows considerable difference in the plume-top height (discussed below). Thus the constraint placed on entrainment by the criteria used here for the match to the observed onset in the temperature–CWV plane is likely complimentary to constraints on entrainment that use cloud-top data (e.g., Brown and Zhang 1997; Bacmeister and Stephens 2010; Luo et al. 2010).

Another measure of deep convective onset diagnosed in the plume model is the updraft vertical velocity. In Fig. 3a we show the 400-hPa plume vertical velocity as a measure of deep convective transition, for the various entrainment cases. Selection of the 400-hPa level to distinguish between the deep cumulonimbus and the

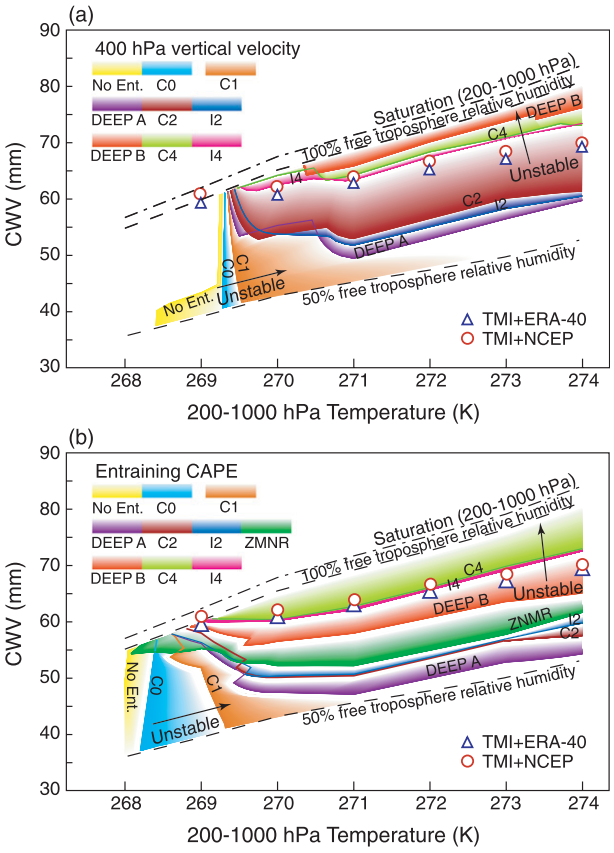

FIG. 3. (a) Onset boundaries as in Fig. 2, but for 5 m s^{-1} contours of 400-hPa vertical velocity. Note that the onset boundary for ZMNR is not shown here, since the vertical velocity is not computed in the scheme. (b) As in Fig. 2, but showing the sensitivity of the onset boundaries with the temperature in the boundary layer (up to 945 hPa) perturbed by 0.5 K, and w_0 (see text) reduced to 5 m s^{-1}.

cumulus congestus is based on some of the recent observational studies (e.g., Luo et al. 2009). It can be seen from Fig. 3a, that similar onset dependence of temperature can be reproduced by using plume vertical velocity as an alternate measure of deep convection for all the entrainment cases except Deep B, which has a lower-tropospheric choke point for lower values of free-tropospheric humidity. In this measure, its onset shifts closer to those of C4 and I4. It is worth noting that the 400 hPa w_u criterion in Fig. 3a more sharply divides the entraining plume models into two families, with Deep A, C2, and I2 onsets occurring at lower CWV than observations. Similar onset boundaries are obtained using the saturation column water vapor over the lower troposphere (550–875 hPa) as an alternate measure of lower-tropospheric temperature (not shown).

Since perturbations in the boundary layer temperature can potentially modulate the deep convective transition characteristics, we perform similar plume computations as above, but with a 0.5-K temperature

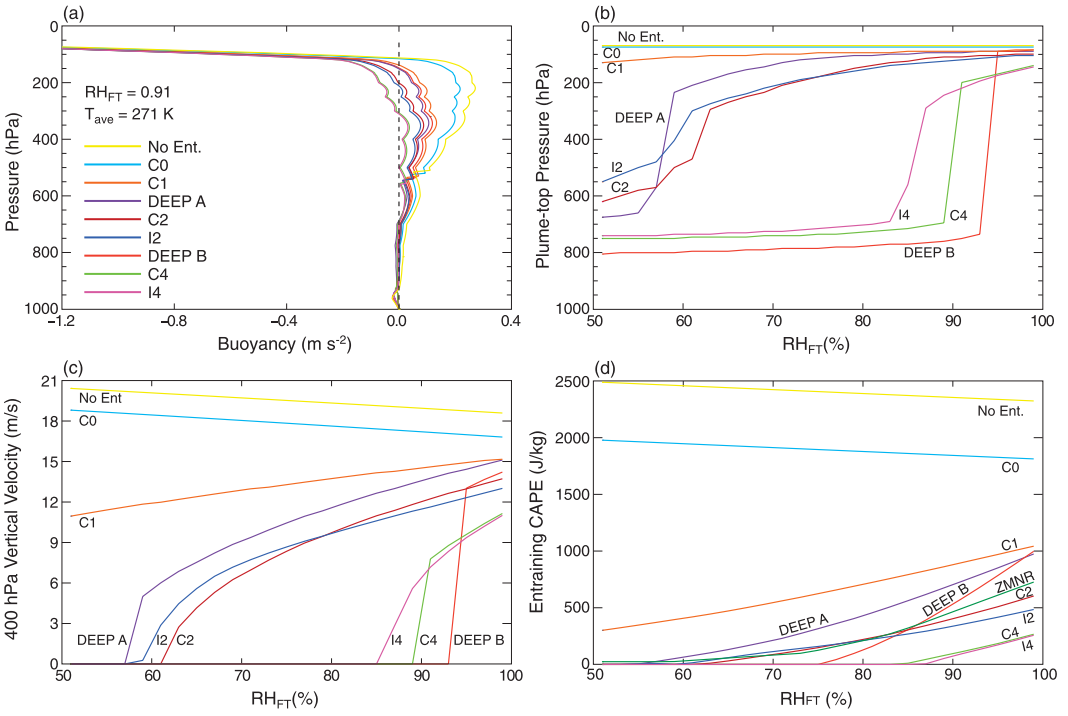

FIG. 4. (a) Parcel buoyancy profiles with various entrainment schemes for free-tropospheric RH = 91%, and $\hat{T} = 271$ K. (b) Plume-top pressures for different values of free-tropospheric RH, and $\hat{T} = 271$ K. (c) As in (b), but showing 400-hPa vertical velocity. (d) As in (b), but showing entraining CAPE (J kg^{-1}) (also includes the computations for ZMNR).

perturbation in the boundary layer (1000–945 hPa) and a reduced initial updraft velocity (w_0 in the updraft vertical velocity equation is set to 5 m s^{-1} instead of 10 m s^{-1}). Entraining CAPE as a function of $\hat{T}$ and CWV is shown in Fig. 3b, similar to Fig. 2 above. It can be seen from the figure that the overall characteristics of the onset boundaries for the various entrainment schemes are similar to Fig. 2. The deep convective onset simply occurs at slightly lower values of CWV and at colder tropospheric temperatures (compared to Fig. 2) for all the cases. Thus, entraining CAPE seems to be a robust measure of the deep convective transition, at least qualitatively.

Another sensitivity test was conducted to verify which levels in the free troposphere are most important in controlling the behavior seen here. One suspects that entrainment in the lower free troposphere will determine whether the plume reaches deep convective levels. Thus we ran a case using C4 values in the lower free troposphere but C2 values in the upper troposphere. Figures comparable to Figs. 2 and 3a (not shown) yield 400-hPa vertical velocity contours almost identical to the C4 case and CAPE contours very close to the C4 case. This reinforces that, as expected, the lower free troposphere is the key layer.

Although the vertical integral of buoyancy is a useful indicator of deep convective onset, details of the vertical buoyancy profile lends important insights into the potential choke points that prevent a plume from undergoing deep convection. In Fig. 4a, we show the buoyancy profiles for the various entrainment schemes for a typical value of free-tropospheric relative humidity (91%) and tropospheric temperature (271 K). For simplicity, freezing is assumed to occur rapidly, so the buoyancy increase associated with freezing can be easily read from the plot as a jump near 500 hPa. While upper-tropospheric buoyancy is larger, the key layers are in the lower troposphere with small buoyancy, where plumes terminate if environmental relative humidity is reduced. It can be seen from the layer of negative buoyancy around 900 hPa in Fig. 4a that there is substantial convective inhibition at the top of the ABL for most of the cases. Even in the subsequent layers up to around 700 hPa, the available buoyancy is very close to zero, and even marginally negative for some of the cases. Thus, the plumes that have enough vertical velocity to cross this inhibition zone make it to the congestus and deep convective levels. Conducive perturbations to the environmental temperature or/and initial vertical velocity of the plume can thus be important for deep convective

onset. Worth noting is the higher cloud-top height in the Deep B case, as compared to C4 and I4, although their onset boundaries look similar. Also interesting to note is that, even though the two deep inflow cases have large differences in their estimated w_c values (see Fig. 2), they are apparently similar in terms of their buoyancy profiles (see Fig. 4a), which can be attributed to the lower-tropospheric choke point present in the case of Deep B plumes.

Using plume-top pressure, plume vertical velocity, and convective instability as measures of deep convection, we examine the dependence of these across the convective onset as a function of free-tropospheric relative humidity (RH_{FT}) for various entrainment assumptions. For these deterministic calculations, we do not expect to reproduce the power-law pickup in precipitation with column water vapor reported in PN06 and NPH09, but simply to obtain a sense of underlying plume properties. It can be seen from Figs. 4b and 4c that there is a pickup in both plume-top pressure and vertical velocity when RH_{FT} exceeds a certain temperature-dependent critical value, only for the high entrainment cases. The cases with low or zero entrainment are unstable for the entire range of free-tropospheric humidity for the given $\hat{T}$ values. From Fig. 4c, it is to be noted that the 400-hPa vertical velocity lines shown in the figure are subject to stochastic broadening, as can be seen from the small jump in vertical velocity for I2, before the occurrence of the actual pickup. Figure 4d shows the entraining CAPE and, as can be seen from the figure, it does not show a corresponding pickup at higher values of RH_{FT}. This is primarily due to the fact that we use the level of neutral buoyancy of the plume to compute the CAPE, which is simply a measure of the accessible amount of energy if the plume is able to undergo deep convective transition, and not the actual energy available to the plume.

b. *Sensitivity to temperature perturbation vertical structure*

We examine the robustness of these onset characteristics in a simpler context. The ERA-40 temperature profiles are replaced by profiles created by adding a set of idealized temperature perturbations to a mean state profile taken from the Department of Energy's Atmospheric Radiation Measurement Program (ARM) radiosonde soundings (Mather et al. 1998) at Nauru from 1 April 2001 to 16 August 2006, averaged over the upper tercile of column water vapor cases, so that cases far from convective onset do not distort the average. In each case the same set of RH perturbations is examined as in section 3a. Plume stability calculations are carried out for the full set of temperature and relative humidity profiles and results are shown in the temperature–CWV plane as before. In a relevant study, Holloway and Neelin (2007, hereafter HN07) used a variety of observations including Atmospheric Infrared Sounder (AIRS) satellite data, radiosonde observations, and NCEP–NCAR reanalysis over the tropics to investigate the dominant vertical structures of temperature perturbations. They found a significant vertical coherence of temperature perturbations in the free troposphere. In addition, the boundary layer was found to be fairly independent of the free troposphere, for smaller spatiotemporal scales. Since the relationship between the boundary layer and the free-tropospheric temperature perturbations depends on the space and time scales, we perform plume computations for both vertically coherent as well as noncoherent perturbation profiles.

1) CONSTANT TEMPERATURE PERTURBATIONS IN BOUNDARY LAYER AND FREE TROPOSPHERE

In this set of plume calculations we assume that the temperature perturbations in the ABL and the free troposphere are vertically coherent, and we apply constant temperature perturbations in the entire atmospheric column (50–1000 hPa). In these experiments, the perturbations are applied to the basic-state tropical sounding from Nauru, described above. Vertically constant temperature perturbations were applied, such that the lapse rate of the atmosphere remains unchanged, with the size of the perturbation varying to change the tropospheric mean temperature through a range of approximately 267.4–274.2 K by intervals of 0.2 K. Although the temperature perturbation differences in ERA-40 vary with height (see the appendix), they tend not to increase with height as a moist adiabat, so a vertically constant temperature perturbation seems as suitable an idealization as any. The relative humidity profile is the same as that used in the previous set of computations.

The results for each entrainment formulation are presented in Fig. 5. The onset boundaries are somewhat simpler than those estimated using reanalysis temperature profiles in Figs. 2 and 3a but maintain very much the same overall features. As was seen earlier, the slope of the onset boundary strongly depends on the value of the mixing coefficient for the constant entrainment calculations, and on the value of the prescribed minimum for the interactive entrainment calculations. As in Fig. 2, the observed w_c–$\hat{T}$ relationship can be approximately captured by the schemes with sufficient entrainment. Overall, this indicates that the behavior is quite robust and can be captured even in simplified conditions.

2) OTHER VARIANTS OF TEMPERATURE PERTURBATIONS IN THE VERTICAL

To further probe the sensitivity of deep convection onset characteristics to temperature perturbation profiles,

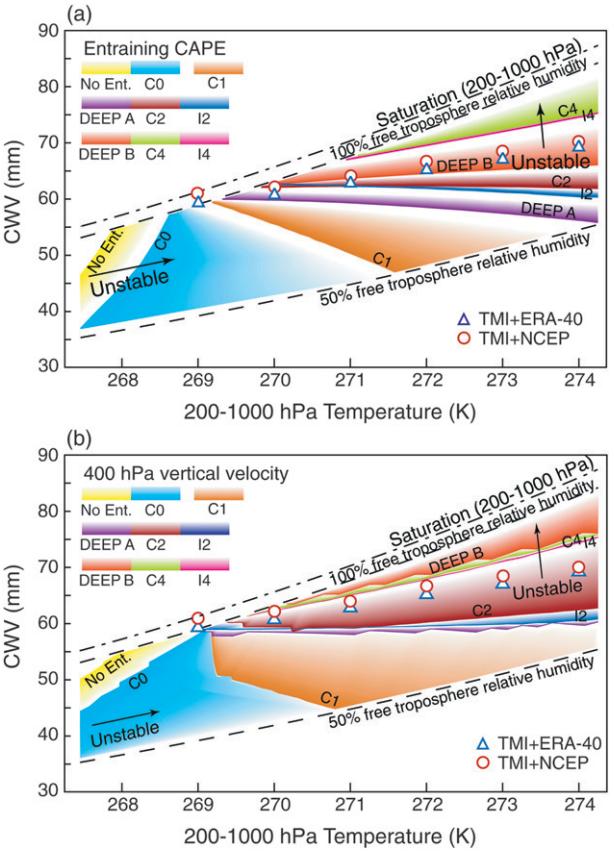

FIG. 5. Onset boundaries for plume calculations as in Figs. 2 and 3a, but with constant temperature perturbations applied to the mean-state temperature sounding over Nauru (see text), in the boundary layer as well as the free troposphere. (a) Entraining CAPE contours of 100 J kg^{-1}; (b) 400-hPa vertical velocity contours of 5 m s^{-1}.

we conduct three more sets of computations. The first case examines the impact of free-tropospheric temperature if the ABL temperature does not change. In the second and third cases, the environmental temperature variations are assumed to be mimicked by those of a convective plume: in the second case with entrainment and in the third case without. This idealization is relevant to the limit in which the vertical dependence of the large-scale tropospheric temperature is dominated by convective processes (neglecting effects such as wave dynamics or radiation). Together, these cases provide a sense of how the behavior depends on different idealizations of the environmental temperature profile variations.

In the first case, we assume that the temperature in the boundary layer and that in the free troposphere vary independently and investigate the role of free-tropospheric temperature (200–950 hPa) in controlling the transition to deep convection. The mean temperature sounding is perturbed in the 50–950-hPa layer, keeping the ABL temperature unchanged. Figure 6a shows the deep convective onset boundaries for this case, for the various entrainment schemes, as a function of $\hat{T}$. The nonentraining case is found to be unstable for the entire range of temperature and relative humidity profiles used and thus does not have an onset boundary in the $\hat{T}$–CWV domain shown in the figure. Even C0 is unstable for most of the domain, similar to that seen in Figs. 2 and 5a, except for the high humidity values at lower temperatures. Onset characteristics with the constant entrainment cases C1, C2, and C4 in Fig. 6a are generally consistent with the results from ERA-40 profiles (Fig. 2) and those obtained with constant perturbation in ABL and free troposphere (Fig. 5a). The onset boundaries of the deep inflow and the interactive entrainment cases, however, behave differently than those seen from earlier plume calculations. For higher values of $\hat{T}$, the onset boundary of Deep B has a slope similar to that estimated from observations, while that of Deep A, I2, and I4 are almost parallel to lines of constant relative humidity. However, for lower values of $\hat{T}$, the onset boundaries for all four cases bend toward much lower values of CWV with decrease in tropospheric temperature. Thus, while the most common behavior encountered in the observed statistics is typified by the case where free troposphere and ABL temperature vary together, when the ABL temperature varies less than that of the free troposphere, it can have significant impacts on the onset boundary. A potential application of this would be to separate such cases in the observations and contrast the onset dependence as a means of providing additional constraints on the entrainment.

In the second case, we perturb the mean temperature sounding with the perturbation profile for a strongly entraining plume, specifically, we use the perturbation profile computed for C4, with $RH_{FT} = 0.75$, and the two $\hat{T}$ values of 270 and 270.2 K (with constant perturbation in the ABL and free troposphere). The onset boundaries for this case are shown in Fig. 6b. Overall, it looks very similar to the results obtained using ERA-40 temperature profiles, although the deep convective onset occurs at somewhat lower values of $\hat{T}$ for most of the entrainment cases.

In the third case, we add moist adiabatic perturbations to the mean-state sounding and construct a similar plot showing onset boundaries for the various entrainment cases. It can be seen from Fig. 6c that the onset boundaries look very different from the ones seen before. For most of the entrainment cases, the onset boundaries cut across lines of constant relative humidity toward somewhat higher values with increasing $\hat{T}$.

Stronger entrainment cases still come closer to the observed onset line than do weaker entrainment cases, but

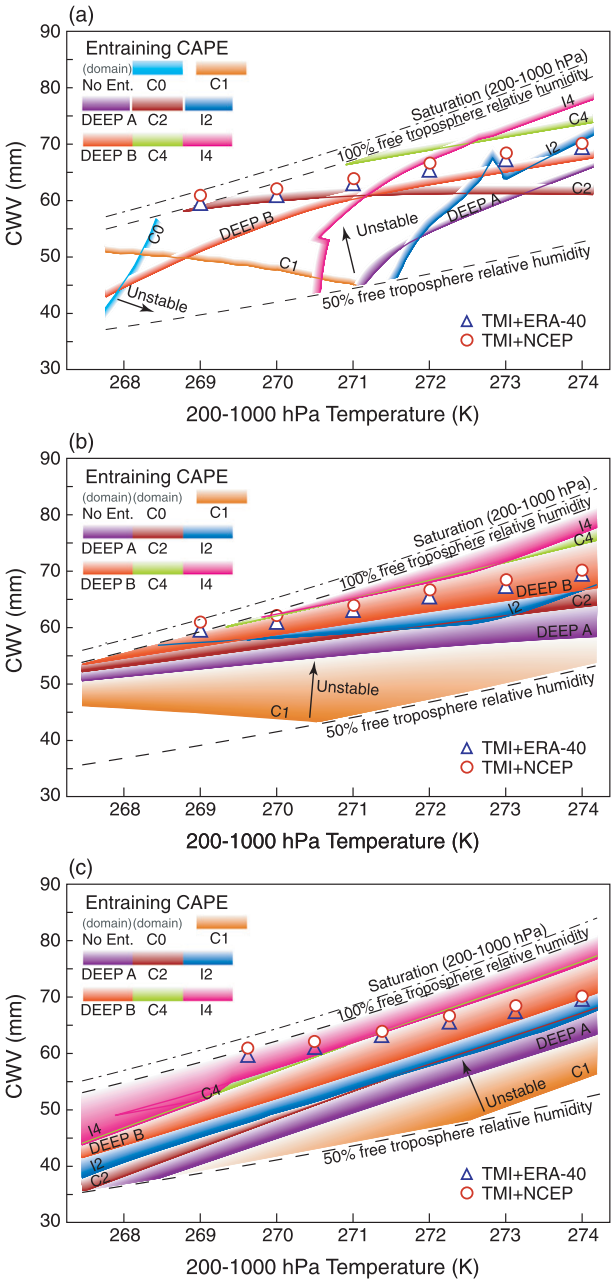

FIG. 6. Entraining CAPE contours of 100 J kg^{-1} as a measure of deep convective onset for the various entrainment cases as in Fig. 5a, but for (a) vertically constant temperature perturbation in the free troposphere, (b) environmental temperature perturbation idealized as for an entraining plume, and (c) environmental temperature perturbation idealized as for a moist adiabat to the mean-state temperature sounding over Nauru. Entrainment cases that are unstable throughout the range of temperature and humidity values used in the study are not shown, and the corresponding color bars have been replaced by the word "domain." The width of the shaded regions is reduced in (a) for graphical clarity because several of the boundaries cross, but this otherwise follows the same convention as Figs. 2, 3, and 5.

the angle does not match the observed boundary. This suggests that the idealization in case 2 (in which both environment and parcel are treated as being affected by entrainment; Fig. 6b) is more self-consistent than case 3, in which the environment was idealized as having changes in tropospheric temperature structure corresponding to a nonentraining case. Comparing these cases to earlier sections, typically Deep A, Deep B, C2, and I2 show similar onset behavior, as do C4 and I4. The exception is the case where temperature perturbations are applied only to the free troposphere (Fig. 6a). Thus, situations where the ABL and the free-tropospheric temperature behave differently appear to yield stronger distinctions among schemes with different vertical dependence of the entrainment coefficient.

4. Usefulness for model analysis

The observed dependence of critical column water vapor on a bulk measure of tropospheric temperature can potentially be used as a constraint for the cumulus parameterization schemes used in general circulation models (GCMs). Here we provide an example of the comparison to microwave retrievals for a widely used atmospheric GCM. The plume stability calculation can likewise be compared to the GCM to aid interpretation. Figure 7 shows precipitation statistics conditionally averaged by 0.3-mm bins of CWV, for 1-K bins of $\hat{T}$ (similar to NPH09), over the tropical eastern and western Pacific Ocean basins, from a moderately high-resolution (0.5°) simulation with the NCAR CAM version 3.5 (Gent et al. 2009), which is closely related to CAM4. This model version has the ZMNR deep convective scheme [the Neale et al. (2008) modification of the Zhang and McFarlane (1995) scheme]. One of the most important aspects of the modification is that an entraining CAPE is used in the closure for the mass flux. As discussed in section 2, the scheme has substantial entrainment through the free troposphere. Similar to Fig. 1a, power-law fit lines are shown for CWV values greater than w_c, with an exponent of 1 for the model output, whereas for TMI it is 0.23 (same as that reported in NPH09). Also overlaid on Fig. 7a are the corresponding values presented in NPH09 (using precipitation and CWV from TMI and tropospheric temperature data from ERA-40).

There are several important pieces of information in this plot. First, the precipitation rates from the model reached fairly high values; that is, at this resolution and for this convective parameterization, the model is far from the low intensity, overly constant rainfall that characterizes some convective schemes. This agrees with the findings of Boyle and Klein (2010), where they

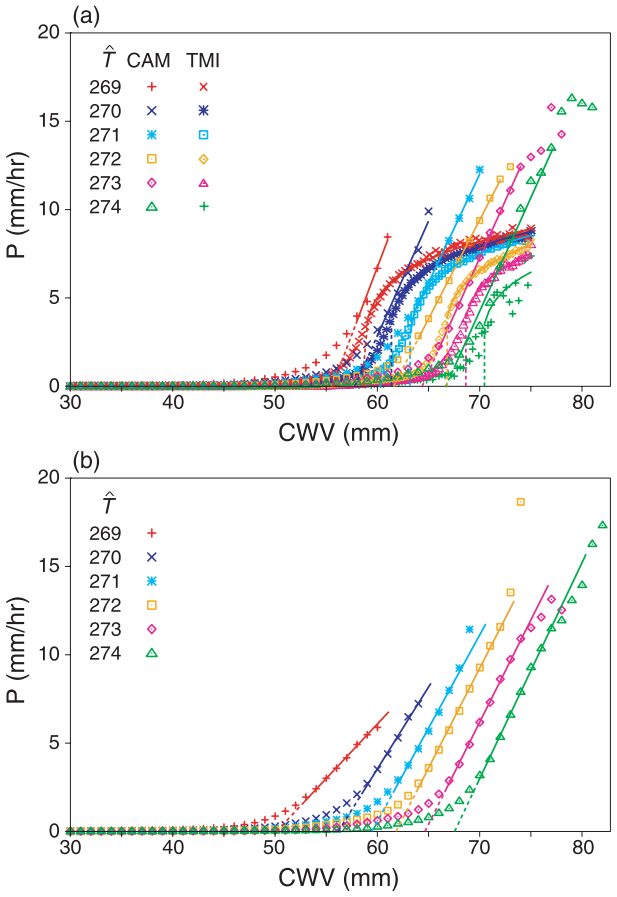

FIG. 7. Precipitation (mm h^{-1}) pickup for different temperature bins from CAM3.5 (0.5°) as a function of CWV: (a) eastern Pacific and (b) western Pacific. Overlaid on (a) are the corresponding values from TMI using ERA-40 temperature profiles. Lines represent power-law fits above the critical value, with an exponent of 1 for the model output, whereas for TMI it is the same as that reported in NPH09.

used CAM4 at varying horizontal resolutions and found that the frequency distribution of rainfall intensity improved at finer resolutions through an increase in frequency of heavy rainfall events as well as in the occurrence of little or no precipitation events. Second, the pickup in precipitation has very reasonable dependence on CWV. The pickup is linear (i.e., a power-law exponent of 1) by the postulates of the convection scheme, and it may be seen that in the region before the linear pickup there is a "foot" region due to the effects of vertical degrees of freedom that are not controlled here, which act like a stochastic broadening. A similar foot occurs in the microwave retrievals before the sharpest part of the pickup (and is well known in statistical mechanics analogs; see discussion in PN06 and NPH09).

In comparing the model and the microwave retrievals in Fig. 7a, the eye is drawn to a difference in curvature at high CWV. The model and microwave curves each fit with a form $a(w - w_c)^{\beta}$ above w_c but they disagree on the value of β. This is left as an open question here because it is unclear to what extent the calibration of the microwave precipitation estimates can be trusted in the high precipitation regime [although Peters et al. (2009) find similar effects in radar retrievals]. Rather, we focus on the temperature dependence of the convective onset. From this point of view, the fit is simply a means of empirically estimating w_c.

For all temperatures and all parts of the curve, the CAM pickup occurs at slightly lower water vapor values than in the observations. However, careful quantification of this and comparison to plume model results suggests that overall the model is doing reasonably well compared to what could occur, and that part of this success can be attributed to the stronger entrainment in the free troposphere. Similar analysis was carried out for the tropical Atlantic and Indian Ocean basins, and the corresponding w_c values were estimated. These estimated w_c values along with the corresponding saturated CWV values for the above ocean basins are shown as a function of $\hat{T}$ in Fig. 8a. It can be seen from the figure that the dependence of w_c on $\hat{T}$ is similar across all the basins, with a roughly linear increase in w_c associated with an increase in $\hat{T}$, but at a rate slower than that of the column saturated value, similar to the findings of NPH09, and those seen from plume calculations above. For the w_c values shown corresponding to $\hat{T} = 269$ K, the lower value for the western Pacific is due to the smaller angle of the linear fit, which is even worse for $\hat{T} = 268$ K (not shown). If one were to compute $\widehat{q_{\rm sat}}$ using unconditioned temperature profiles, we note that the values for the Atlantic at 273 and 274 K, and for the Indian Ocean at 274 K, are substantially higher in the CAM than the other basins or observations because of the occasional occurrence of warm low-level conditions that are also dry and have no chance of convecting (not shown). The $\widehat{q_{\rm sat}}$ values shown in Fig. 8a are computed for CWV values high enough that the temperature profile is relevant to the convective onset. Specifically, the average is for temperature profiles with CWV greater than $38 + 15(\hat{T} - 268)/6$, which roughly approximates $0.8w_c$. The w_c values for the Atlantic could not be estimated for $\hat{T}$ values of 273–274 K.

To further quantify the comparison of the observed results and those from the plume calculations with the ZMNR scheme, offline calculations using ZMNR with similar profiles of temperature and moisture to those used for the plume calculations were carried out. Entraining CAPE contours of 70 and 100 J kg^{-1} are shown in Fig. 8b. Note that much of the information is repeated from Figs. 2 and 8a for comparison. The 100 J kg^{-1} contour runs very close to w_c values estimated from the

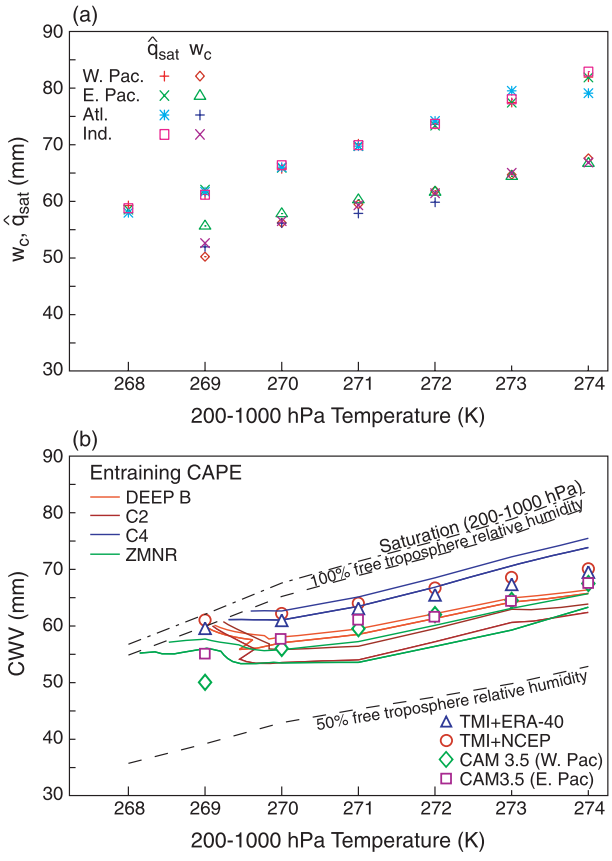

FIG. 8. (a) Critical values w_c and saturation values of column water vapor $\widehat{q_{sat}}$ (mm) as a function of mean tropospheric temperature (K) for different ocean basins, from CAM3.5 (0.5°). (b) The w_c values over the tropical eastern and western Pacific as a function of CWV and $\hat{T}$. Also shown are the w_c values for the western Pacific, obtained from TMI binned by NCEP $\hat{T}$, and ERA-40 $\hat{T}$ (repeated from Fig. 2). Entraining CAPE contours of 70 and 100 J kg^{-1} are shown for Deep B, C2, and C4 from the plume calculations, and from offline computations using the ZMNR scheme used in CAM3.5.

precipitation onset statistics in CAM3.5 for all of the temperatures except the lowest bin. The 70 J kg^{-1} contour parallels this, shifted a few millimeters toward lower CWV. Combining this with information from the CAPE and precipitation pickup curves in Figs. 4 and 7, we can infer some factors affecting quantitative comparison to observations. The model convective onset inferred from the precipitation statistics in most respects agrees very well with the model onset inferred from the ZMNR plume calculation, supporting the usefulness of quantitative comparison between these. A caveat may be seen at the lowest temperature, where the model w_c estimate is noticeably affected by the flattening by stochastic effects in the foot of the $\hat{T} = 269$ K curve in the western Pacific. Indicators of this behavior include the lack of distinction between the upward curving and linear portion of the $\hat{T} = 269$ K curve in Fig. 7b, the difference in slope between this curve and those for other $\hat{T}$ values, and the disagreement in w_c values for different basins at $\hat{T} = 269$ K in Fig. 8a.

The precipitation-estimated onset in CAM3.5 is more closely matched by the 100 J kg^{-1} contour in plume calculations than by the 70 J kg^{-1} contour despite the fact that in ZMNR cloud-base mass flux increases linearly above a CAPE threshold of 70 J kg^{-1}. This likely reflects differences in details of the CAM3.5 vertical structure compared to the ERA-40 based profiles used in the plume calculations (possibly combined with differences in the parameterized precipitation pickup from that of CAPE). This serves as a reminder that differences between model and observed onset boundaries need not be purely due to factors within the deep convection scheme. We note that for other entrainment schemes that are reasonably close to matching the observed onset, C2, C4, and Deep B, the offset between 70 and 100 J kg^{-1} is smaller (Fig. 8b). The results suggest that the increased entrainment of ZMNR relative to the standard Zhang–McFarlane scheme has been highly beneficial in yielding results close to observations in these measures. However, the differences between the steepness of the onset in upper-tropospheric vertical velocity compared to the slow onset in CAPE hint that changes in the form of the parameterization may also be worth considering.

From these results, it is tempting to suggest that an alteration of the entrainment assumptions might further improve the model's match to the location of the onset in the temperature–water vapor plane. However, even if one can deliver the correct convective response to the temperature/humidity states (in terms of the critical value of onset) as a function of entrainment in offline mode, there is no guarantee that, in the model, this will deliver the correct frequency of a particular temperature/humidity state. For instance, feedbacks that tend to humidify the environment are encountered when entrainment is further increased in CAM3.5. Thus, it is worth underlining that these statistics are among the many that must be used to constrain a model.

5. Discussion

The ability of a simple plume model to reproduce and explain conditional mean characteristics of the observed transition to deep convection is examined using various entrainment assumptions. Results for the convective onset in a relatively high-resolution GCM with parameterized convection are then compared both to observations and to the plume calculations. In the plume model, two measures of the onset of deep convection via

conditional instability are examined: entraining CAPE (from a very standard parcel computation) and plume vertical velocity diagnosed from buoyancy via the simple plume model.

The behavior is examined in a temperature–water vapor thermodynamic plane, using column water vapor and tropospheric vertically averaged temperature $\hat{T}$ because these can be compared to the onset of strong precipitation as previously estimated in satellite retrievals. Plume calculations using ERA-40 temperature profiles yield deep convective onset characteristics that are strongly affected by entrainment assumptions. The threshold value of CWV above which there is an abrupt increase in precipitation, referred to as the critical CWV, is found to increase with mean tropospheric temperature, but at a rate slower than the column saturation, as in observations, only for the cases with high or moderately high fractional entrainment rates. Low entrainment rates yield a curve for the onset of conditional instability that is very different from the observed curve for the onset of strong precipitation.

This result has a number of consequences.

(i) First, it confirms the assumption in PN06 and NPH09 that certain basic features of the observed statistics for the transition to strong tropical precipitation are associated with the onset of conditional instability through a deep convective layer, and that these can be captured by conventional parcel or plume representations as initially examined in HN09.
(ii) Second, this permits exploration of the factors that set the empirically determined onset boundary as a function of temperature and moisture.
(iii) Third, it places additional observational constraints on the entrainment representation in the convective schemes and helps to quantify the dependence of the onset of the convection on free-tropospheric moisture, providing further evidence that this arises by entrainment in the lower free troposphere.
(iv) Finally, it provides additional validation metrics for climate model performance on the onset of deep convection.

We elaborate on each of these below.

Regarding (i), one should distinguish between properties that one does or does not expect to be captured by parcel or plume calculations. The dependence of the onset boundary on temperature and moisture is an important property that can be captured by individual plume calculations. More challenging properties of the set identified in observations (PN06; NPH09), such as power-law spatial correlation, cannot. The plume results here are consistent with the conjecture (Neelin et al. 2008) that convective plumes may be suitable microscale entities for calculations that include neighbor plume–plume interactions and stochastic interactions with microphysics and turbulence to capture the additional properties in convective schemes. The form of the pickup in convective onset variables (such as precipitation or buoyancy-based measures) should depend on both the form of the pickup for an individual plume and the neighbor or stochastic interactions (NPH09; Muller et al. 2009). Here, dependence of the plume-top height and the 400-hPa vertical velocity on free-tropospheric humidity shows a sharp pickup similar to that seen in observational radar and microwave precipitation retrievals, provided entrainment is sufficiently high. The sharp transition is associated with a rapid change from plumes that terminate at trade cumulus or congestus levels to deep convection. Entraining CAPE, however, shows an approximately linear pickup, since the integrated buoyancy (from the surface to the level of neutral buoyancy of the plume) evolves relatively smoothly as free-tropospheric moisture increases for a given temperature profile. The quantitative nature of the pickup in models may thus be expected to depend fairly sensitively on parameterized dependence of precipitation microphysics on vertical velocity, mass flux, or buoyancy.

Regarding (ii), in addition to the strong dependence on properties that can be regarded as internal to the convective elements, such as entrainment, the convective onset does naturally have a dependence on how the large-scale temperature profile varies as its vertical average (or other bulk measure) increases in observations. Sensitivity tests using simplifying assumptions regarding the perturbation profile (i.e., the departure of environmental temperature from a typical mean temperature sounding) may be summarized as follows. Convective onset dependence on temperature and moisture similar to those found in the ERA-40 case can be obtained for cases where the environmental temperature changes are applied to the boundary layer and the free troposphere and have little vertical structure (e.g., are constant in the vertical or mimic the perturbation structure of a strongly entraining plume). If the environmental temperature structure instead increases with height like a moist adiabat, the angles of the onset boundary change substantially in the temperature–moisture plane (under this simplifying circumstance parts of the onset boundary become closer to lines of constant relative humidity, although they still depart significantly from this for cases with convective onset at lower relative humidity). When the environmental temperature changes in the free troposphere but not in the boundary layer, onset boundaries change substantially (relative to ERA-40 cases) for some entrainment schemes but not others, indicating a greater sensitivity to the vertical structure of the assumed

entrainment. This suggests that it should be possible to find regional or seasonal dependence in the onset boundary that reflects this sensitivity. Controlling for additional vertical degrees of freedom, especially boundary versus lower free troposphere, in the temperature and water vapor while estimating the deep convective onset boundary may then provide additional constraints on entrainment assumptions.

Regarding (iii), the sensitivity to entrainment strongly suggests that low entrainment cases are inconsistent with observations in the deep convective onset measures used here. This reinforces HN09's results as a function of CWV from Nauru data and is consistent with findings that intraseasonal variability is better simulated if a minimum entrainment rate is enforced (Tokioka et al. 1988; Lee et al. 2003). Different vertical structures of the entrainment rate can match the observed onset boundary, provided they have sufficient entrainment in the lower free troposphere, which is the key layer here. In terms of practical applications, this has the benefit that one does not have to fully settle the question of vertical dependence of the entrainment coefficient to match this important feature of observations. On the other hand, it does imply that other criteria would have to be added to constrain the vertical dependence of the entrainment. The onset boundary constraint is sufficiently independent of criteria such as cloud-top height that combining these constraints could yield additional information. It is worth underlining that there is no need for an explicit dependence of the entrainment coefficient on moisture to match the observed sensitivity of the convective onset to free-tropospheric moisture in the measures used here. It is sufficient that the entrainment rate be large enough in the lower free troposphere. The dependence on free-tropospheric moisture arises simply by entrainment of lower free-tropospheric air; if this layer is too dry the resulting loss of buoyancy produces trade cumulus or congestus instead of deep convection.

An additional simplifying consideration comes from examination of a simple interactive entrainment scheme, in which a prescribed turbulent component of total entrainment is augmented by a dynamic component (associated with buoyancy-induced vertical acceleration). The onset of deep convection proves to be strongly governed by the minimum (i.e., turbulent) entrainment. The contribution of the dynamic component to the total entrainment in most cases makes no significant difference to the temperature dependence of the onset. The buoyancy near onset is simply too small to drive much dynamic entrainment; for the large values of the turbulent entrainment coefficient required to match the observed onset boundary, this remains true through most of the domain. Contrary to initial expectations, investment in dynamic entrainment schemes thus does not appear to be a high priority.

Regarding (iv), analysis of data from a moderately high-resolution (0.5°) model integration using the NCAR CAM3.5 suggests that the model does well enough in these rainfall statistics for quantitative comparison to be useful. As expected, the simulated pickup shows a linear dependence on CWV, unlike the power-law pickup seen in microwave retrievals, due to the assumptions in the convective closure, but simulated rainfall rates do reach high values, unlike the low-intensity drizzle associated with some cumulus schemes. The temperature dependence of the precipitation pickup exhibits encouragingly good agreement between the model and observations. The critical CWV for the precipitation pickup is slightly lower for the model than that estimated from observations. There is some dependence on the method for estimating the critical value, given the differences in the form of the pickup, but the tendency for the model to yield a given value of conditionally averaged precipitation at a lower CWV can also be seen directly by comparing the pickup plots. The model output also permits verification that there is a reasonable agreement in the temperature–water vapor dependence of the convective onset obtained from precipitation calculations with that obtained for buoyancy in the offline simulations performed using the convection scheme of the model. Overall, the level of agreement suggests that these precipitation statistics, including the deep convective onset curves in the temperature–water vapor plane, can provide a strong constraint for high-resolution GCMs.

Acknowledgments. This work was supported in part by National Science Foundation Grant AGS-1102838, National Oceanic and Atmospheric Administration Grant NA11OAR4310099 and Department of Energy Grant DE-SC0006739. We thank J. E. Meyerson for graphical assistance.

APPENDIX

ERA-40 Temperature Profile Differences and Entrainment Profiles

A significant vertical coherence in tropical temperature perturbations in the free troposphere was reported in HN07, using observations from various datasets, including AIRS satellite data, radiosonde observations, and the NCEP–NCAR reanalysis. They found that the temperature perturbations in the boundary layer are fairly independent of that in the free troposphere; however, this relationship was found to have a spatiotemporal

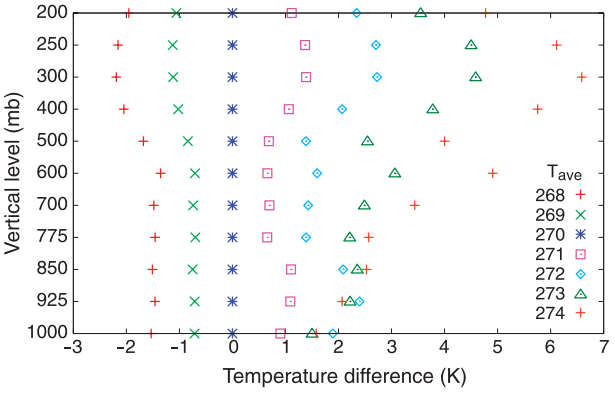

FIG. A1. Vertical temperature perturbation profile over the tropical western Pacific, using ERA-40, for the period 1998–2001, using $\hat{T} = 270$ K as the base profile from which the differences are computed.

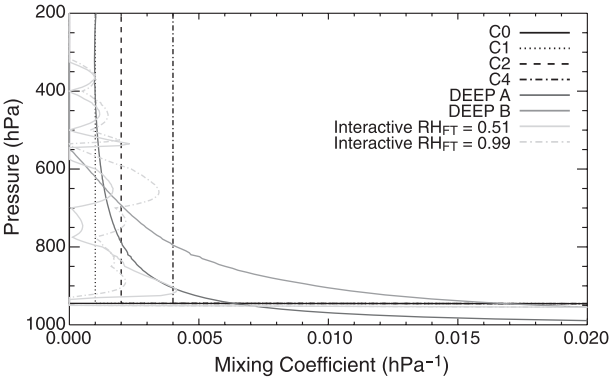

FIG. A2. Vertical profile of mixing coefficient for the various entrainment schemes. The mixing coefficient for the interactive scheme is illustrated for a temperature profile from ERA-40 with $\hat{T} = 271$ K, using the case where 0.5 K was added in the ABL (see text), and for two extreme values of free-tropospheric relative humidity used in this study (51% and 99%).

scale dependence. To investigate the vertical structure of temperature perturbations over the tropical western Pacific (the region of interest), we use the ERA-40 temperature profiles. These temperature profiles were first binned at 1-K intervals of $\hat{T}$, and then the mean profile for each bin was computed. To calculate the vertical temperature perturbation profile for each of the bins, the mean for the 270-K $\hat{T}$ bin was chosen as a base profile and was subtracted from the corresponding mean profile of the other bins. The vertical profiles of temperature perturbations, thus computed, are shown in Fig. A1, and it can be seen from the figure that, while for some of the bins the boundary layer and the free troposphere are vertically coherent (e.g., the 269-K bin), for other bins they appear to be fairly independent (e.g., the 274-K bin). Thus, both scenarios of vertical temperature perturbation dependence need to be explored in any such sensitivity study of the type discussed in section 3b of the text.

In Fig. A2, we show the mixing coefficient profiles for the different entrainment schemes. The constant entrainment schemes (C0, C1, C2, and C4) have a high value (0.18 hPa^{-1}) in the ABL and a much lower value (0, 1, 2, and 4×10^{-3} hPa^{-1}, respectively) for the rest of the vertical column. For the deep inflow schemes, Deep A has an inverse dependence on height [computed in z coordinates, see Eq. (2)] at all levels. Deep B likewise has approximately a z^{-1} dependence at the lowest levels but with a larger coefficient, so it drops off more slowly, thus leading to stronger entrainment in the lower troposphere, and tapers to zero at midlevels. The interactive scheme is shown for $\hat{T} = 271$ K, using the case of 0.5 K added in the ABL (which illustrates the largest low-level entrainment) and two extreme values of free-tropospheric humidity (RH_{FT}) of 51% and 99%. Cases with no minimum entrainment are shown, where the mixing is purely dynamic, driven by the updraft vertical acceleration. When a minimum entrainment is included, the dynamic contribution can change, but it tends to follow a similar vertical structure. The mixing coefficient exhibits strong vertical variations that also change depending on the environment. For the $RH_{FT} = 0.51$ case, there is no dynamic entrainment in the convective inhibition layer near 950 hPa at the top of the ABL, since there is no positive vertical acceleration. Substantial entrainment occurs in the 930–800-hPa layer, where the plume is subject to strong vertical acceleration, but above this the entrainment drops to typically smaller values. This region of low entrainment in the free troposphere permits plume instability even at these low humidity values. The entrainment coefficient is larger in this layer for $RH_{FT} = 0.99$, but at high relative humidity it has less effect on the parcel. Thus, specifying a minimum entrainment is important for the interactive scheme, as this leads to enhanced mixing in the lower troposphere, making the plume more sensitive to the environmental conditions.

REFERENCES

Austin, J. M., 1948: A note on cumulus growth in a nonsaturated environment. *J. Meteor.,* **5,** 103–107.

Bacmeister, J. T., and G. L. Stephens, 2010: Spatial statistics of likely convective clouds in CloudSat data. *J. Geophys. Res.,* **116,** D04104, doi:10.1029/2010JD014444.

Bechtold, P., M. Köhler, T. Jung, F. Doblas-Reyes, M. Leutbecher, M. J. Rodwell, F. Vitart, and G. Balsamo, 2008: Advances in simulating atmospheric variability with the ECMWF model: From synoptic to decadal time-scales. *Quart. J. Roy. Meteor. Soc.,* **134,** 1337–1351, doi:10.1002/qj.289.

Boyle, J., and S. A. Klein, 2010: Impact of horizontal resolution on climate model forecasts of tropical precipitation and diabatic heating for the TWP-ICE period. *J. Geophys. Res.,* **115,** D23113, doi:10.1029/2010JD014262.

Bretherton, C. S., M. E. Peters, and L. E. Back, 2004: Relationships between water vapor path and precipitation over the tropical oceans. *J. Climate,* **17,** 1517–1528.

Brown, R. G., and C. Zhang, 1997: Variability of midtropospheric moisture and its effect on cloud-top height distribution during TOGA COARE. *J. Atmos. Sci.,* **54,** 2760–2774.

Cifelli, R., and S. Rutledge, 1994: Vertical motion structure in maritime continent mesoscale convective systems: Results from a 50-MHz profiler. *J. Atmos. Sci.,* **51,** 2631–2652.

Derbyshire, S. H., I. Beau, P. Bechtold, J.-Y. Grandpeix, J.-M. Piriou, J.-L. Redelsperger, and P. M. M. Soares, 2004: Sensitivity of moist convection to environmental humidity. *Quart. J. Roy. Meteor. Soc.,* **130,** 3055–3079.

de Rooy, W. C., and A. P. Siebesma, 2010: Analytical expressions for entrainment and detrainment in cumulus convection. *Quart. J. Roy. Meteor. Soc.,* **136,** 1216–1227, doi:10.1002/qj.640.

Ferrier, B. S., and R. A. Houze, 1989: One-dimensional time-dependent modeling of GATE cumulonimbus convection. *J. Atmos. Sci.,* **46,** 330–352.

Gent, P. R., S. Yeager, R. B. Neale, S. Levis, and D. Bailey, 2009: Improvements in a half degree atmosphere/land version of the CCSM. *Climate Dyn.,* **34,** 819–833, doi:10.1007/s00382-009-0614-8.

Grabowski, W. W., 2003: MJO-like coherent structures: Sensitivity simulations using the cloud-resolving convection parameterization (CRCP). *J. Atmos. Sci.,* **60,** 847–864.

Gregory, D., 2001: Estimation of entrainment rate in simple models of convective clouds. *Quart. J. Roy. Meteor. Soc.,* **127,** 53–72, doi:10.1002/qj.49712757104.

Hilburn, K. A., and F. J. Wentz, 2008: Intercalibrated passive microwave rain products from the Unified Microwave Ocean Retrieval Algorithm (UMORA). *J. Appl. Meteor. Climatol.,* **47,** 778–794.

Holloway, C. E., and J. D. Neelin, 2007: The convective cold top and quasi equilibrium. *J. Atmos. Sci.,* **64,** 1467–1487.

——, and ——, 2009: Moisture vertical structure, column water vapor, and tropical deep convection. *J. Atmos. Sci.,* **66,** 1665–1683.

Houghton, H. G., and H. E. Cramer, 1951: A theory of entrainment in convective currents. *J. Meteor.,* **8,** 95–102.

Jensen, M. P., and A. D. Del Genio, 2006: Factors limiting convective cloud-top height at the ARM Nauru Island Climate Research Facility. *J. Climate,* **19,** 2105–2117.

Kalnay, E., and Coauthors, 1996: The NCEP/NCAR 40-Year Reanalysis Project. *Bull. Amer. Meteor. Soc.,* **77,** 437–471.

Kim, D., and I. S. Kang, 2012: A bulk mass flux convection scheme for climate model: Description and moisture sensitivity. *Climate Dyn.,* **38,** 411–429, doi:10.1007/s00382-010-0972-2.

Kuang, Z., and C. S. Bretherton, 2006: A mass-flux scheme view of a high-resolution simulation of a transition from shallow to deep cumulus convection. *J. Atmos. Sci.,* **63,** 1895–1909.

Kummerow, C., and Coauthors, 2000: The status of the Tropical Rainfall Measuring Mission (TRMM) after two years in orbit. *J. Appl. Meteor.,* **39,** 1965–1982.

Lee, M. I., I. S. Kang, and B. E. Mapes, 2003: Impacts of cumulus convection parameterization on aqua-planet AGCM simulations of tropical intraseasonal variability. *J. Meteor. Soc. Japan,* **81,** 963–992.

LeMone, M. A., and E. J. Zipser, 1980: Cumulonimbus vertical velocity events in GATE. Part I: Diameter, intensity and mass flux. *J. Atmos. Sci.,* **37,** 2444–2457.

——, and M. W. Moncrieff, 1994: Momentum and mass transport by convective bands: Comparisons of highly idealized dynamical models to observations. *J. Atmos. Sci.,* **51,** 281–305.

Li, Y., E. J. Zipser, S. K. Krueger, and M. A. Zulauf, 2008: Cloud-resolving modeling of deep convection during KWAJEX. Part I: Comparison to TRMM satellite and ground-based radar observations. *Mon. Wea. Rev.,* **136,** 2699–2712.

Luo, Z., G. Y. Liu, G. L. Stephens, and R. H. Johnson, 2009: Terminal versus transient cumulus congestus: A Cloudsat perspective. *Geophys. Res. Lett.,* **36,** L05808, doi:10.1029/2008GL036927.

——, ——, and ——, 2010: Use of A-Train data to estimate convective buoyancy and entrainment rate. *Geophys. Res. Lett.,* **37,** L09804, doi:10.1029/2010GL042904.

Malkus, J. S., 1954: Some results of a trade-cumulus cloud investigation. *J. Meteor.,* **11,** 220–237.

Mather, J. H., T. P. Ackerman, W. E. Clements, F. J. Barnes, M. D. Ivey, L. D. Hatfield, and R. M. Reynolds, 1998: An atmospheric radiation and cloud station in the tropical western Pacific. *Bull. Amer. Meteor. Soc.,* **79,** 627–642.

Muller, C. J., L. E. Back, P. A. O'Gorman, and K. A. Emanuel, 2009: A model for the relationship between tropical precipitation and column water vapor. *Geophys. Res. Lett.,* **36,** L16804, doi:10.1029/2009GL039667.

Neale, R. B., J. H. Richter, and M. Jochum, 2008: The impact of convection on ENSO: From a delayed oscillator to a series of events. *J. Climate,* **21,** 5904–5924.

Neelin, J. D., O. Peters, J. W.-B. Lin, K. Hales, and C. E. Holloway, 2008: Rethinking convective quasi-equilibrium: Observational constraints for stochastic convective schemes in climate models. *Philos. Trans. Roy. Soc.,* **366A,** 2579–2602.

——, ——, and K. Hales, 2009: The transition to strong convection. *J. Atmos. Sci.,* **66,** 2367–2384.

——, A. Bracco, H. Luo, J. C. McWilliams, and J. E. Meyerson, 2010: Considerations for parameter optimization and sensitivity in climate models. *Proc. Natl. Acad. Sci.,* **107,** 21 349–21 354, doi:10.1073/pnas.1015473107.

Parsons, D. B., K. Yoneyama, and J.-L. Redelsperger, 2000: The evolution of the tropical western Pacific atmosphere–ocean system following the arrival of a dry intrusion. *Quart. J. Roy. Meteor. Soc.,* **126,** 517–548.

Peters, O., and J. D. Neelin, 2006: Critical phenomena in atmospheric precipitation. *Nat. Phys.,* **2,** 393–396, doi:10.1038/nphys314.

——, ——, and S. W. Nesbitt, 2009: Mesoscale convective systems and critical clusters. *J. Atmos. Sci.,* **66,** 2913–2924.

Raymond, D. J., and A. M. Blyth, 1986: A stochastic mixing model for nonprecipitating cumulus clouds. *J. Atmos. Sci.,* **43,** 2708–2718.

Robe, F. R., and K. A. Emanuel, 1996: Moist convective scaling: Some inferences from three-dimensional cloud ensemble simulations. *J. Atmos. Sci.,* **53,** 3265–3275.

Romps, D., and Z. Kuang, 2010: Do undiluted convective plumes exist in the upper tropical troposphere? *J. Atmos. Sci.,* **67,** 468–484.

Sherwood, S. C., 1999: Convective precursors and predictability in the tropical Western Pacific. *Mon. Wea. Rev.,* **127,** 2977–2991.

——, T. Horinouchi, and H. A. Zeleznik, 2003: Convective impact on temperatures observed near the tropical tropopause. *J. Atmos. Sci.,* **60,** 1847–1856.

Siebesma, A. P., P. M. M. Soares, and J. Teixeira, 2007: A combined eddy-diffusivity mass-flux approach for the convective boundary layer. *J. Atmos. Sci.,* **64,** 1230–1248.

Simpson, J., and V. Wiggert, 1969: Models of precipitating cumulus towers. *Mon. Wea. Rev.,* **97,** 471–489.

Stainforth, D. A., and Coauthors, 2005: Uncertainty in predictions of the climate response to rising levels of greenhouse gases. *Nature,* **433,** 403–406.

Sud, Y. C., and G. K. Walker, 1999: Microphysics of clouds with the relaxed Arakawa–Schubert scheme (McRAS). Part II: Implementation and performance in GEOS II GCM. *J. Atmos. Sci.,* **56,** 3221–3240.

Tiedtke, M., 1989: A comprehensive mass flux scheme for cumulus parameterization in large-scale models. *Mon. Wea. Rev.,* **117,** 1779–1800.

Tokioka, T., K. Yamazaki, A. Kitoh, and T. Ose, 1988: The equatorial 30–60 day oscillation and the Arakawa–Schubert penetrative cumulus parameterization. *J. Meteor. Soc. Japan,* **66,** 883–901.

Tompkins, A. M., 2001: Organization of tropical convection in low vertical wind shears: The role of cold pools. *J. Atmos. Sci.,* **58,** 1650–1672.

Uppala, S. M., and Coauthors, 2005: The ERA-40 Re-Analysis. *Quart. J. Roy. Meteor. Soc.,* **131,** 2961–3012, doi:10.1256/qj.04.176.

Wakimoto, R. M., 1982: The life cycle of thunderstorm gust fronts as viewed with Doppler radar and rawinsonde data. *Mon. Wea. Rev.,* **110,** 1060–1082.

Zhang, G. J., 2009: Effects of entrainment on convective available potential energy and closure assumptions in convection parameterization. *J. Geophys. Res.,* **114,** D07109, doi:10.1029/2008JD010976.

——, and N. A. McFarlane, 1995: Sensitivity of climate simulations to the parameterization of cumulus convection in the Canadian Climate Centre general circulation model. *Atmos.–Ocean,* **33,** 407–446.

Zhao, M., I. M. Held, S. J. Lin, and G. A. Vecchi, 2009: Simulations of global hurricane climatology, interannual variability, and response to global warming using a 50-km resolution GCM. *J. Climate,* **22,** 6653–6678.